Available online at www.sciencedirect.com
SCIENCE DIRECT®
Cement & Concrete Composites 28 (2006) 370–383
Cement & Concrete Composites
www.elsevier.com/locate/cemconcomp

Nondestructive testing of concrete with electromagnetic and elastic waves: Modeling and imaging

K.J. Langenberg *, K. Mayer, R. Marklein

Department of Electrical Engineering and Computer Science, University of Kassel, D-34109 Kassel, Germany

Available online 31 March 2006

Abstract

The theory of acoustic, electromagnetic and elastic wave fields in terms of governing equations, plane waves, spherical waves (Green functions) and scattered field representations is discussed under common aspects leading to a unified derivation of modeling and imaging algorithms. The latter require a linearization of the inverse scattering problem. Applications referring to the location and assessment of tendon ducts in concrete are presented utilizing synthetic as well as experimental data culminating in a real-life example for data taken from a bridge.
© 2006 Elsevier Ltd. All rights reserved.

Keywords: NDT; Acoustic, electromagnetic, elastic waves; Unified derivation; Modeling and imaging algorithms; Inverse scattering; Tendon ducts; Concrete; Bridge testing

1. Introduction

We consider the problem to locate and assess tendon ducts in concrete as a specific task in nondestructive testing of concrete. As an example, Fig. 1 shows the making of a test specimen: A tendon duct has been placed below a steel reinforcement and the picture has been taken while the concrete is poured in. Obviously, concrete principally allows for the propagation of electromagnetic as well as acousto-elastic waves, and, hence, both wave modes can be utilized to solve the task locating the duct below the reinforcement and assessing its integrity, i.e., identifying grouting defects. Electromagnetic waves face the problem of being shielded by the steel grid and the duct itself whereas elastic waves are strongly affected by the inhomogeneity of the concrete composition. Hence, it is advisable to investigate the wave propagation in terms of a parametric study applying numerical codes to solve the respective underlying wave equations; the similarity of the latter then suggests the formulation of a unified theory of inversion and imaging.

* Corresponding author. Tel.: +49 561 804 6368; fax: +49 561 804 6489.
E-mail address: langenberg@uni-kassel.de (K.J. Langenberg).

0958-9465/$ - see front matter © 2006 Elsevier Ltd. All rights reserved.
doi:10.1016/j.cemconcomp.2006.02.010

2. Electromagnetic and acousto-elastic waves

2.1. Governing equations

2.1.1. Electromagnetic waves

As it is well-known, the propagation of electromagnetic waves is predicted and governed by Maxwell's curl equations [1]

$$\frac{\partial \underline{\mathbf{D}}(\underline{\mathbf{R}},t)}{\partial t} = \nabla \times \underline{\mathbf{H}}(\underline{\mathbf{R}},t) - \underline{\mathbf{J}}_{\mathrm{e}}(\underline{\mathbf{R}},t), \tag{2.1}$$

$$\frac{\partial \underline{\mathbf{B}}(\underline{\mathbf{R}},t)}{\partial t} = -\nabla \times \underline{\mathbf{E}}(\underline{\mathbf{R}},t) - \underline{\mathbf{J}}_{\mathrm{m}}(\underline{\mathbf{R}},t) \tag{2.2}$$

complemented by compatibility equations

$$\nabla \cdot \underline{\mathbf{D}}(\underline{\mathbf{R}},t) = \varrho_{\mathrm{e}}(\underline{\mathbf{R}},t), \tag{2.3}$$

$$\nabla \cdot \underline{\mathbf{B}}(\underline{\mathbf{R}},t) = \varrho_{\mathrm{m}}(\underline{\mathbf{R}},t). \tag{2.4}$$

Time derivatives of electric and magnetic flux densities—vectors $\underline{\mathbf{D}}(\underline{\mathbf{R}},t)$ and $\underline{\mathbf{B}}(\underline{\mathbf{R}},t)$—at a certain point in space characterized by the vector of position $\underline{\mathbf{R}}$ yield curl densities in terms of the cross(vector)-product of the del-operator ∇ with the respective field-strengths $\underline{\mathbf{H}}(\underline{\mathbf{R}},t)$ (magnetic field strength) and $\underline{\mathbf{E}}(\underline{\mathbf{R}},t)$ (electric field strength); it is understood that the electromagnetic field is generated by

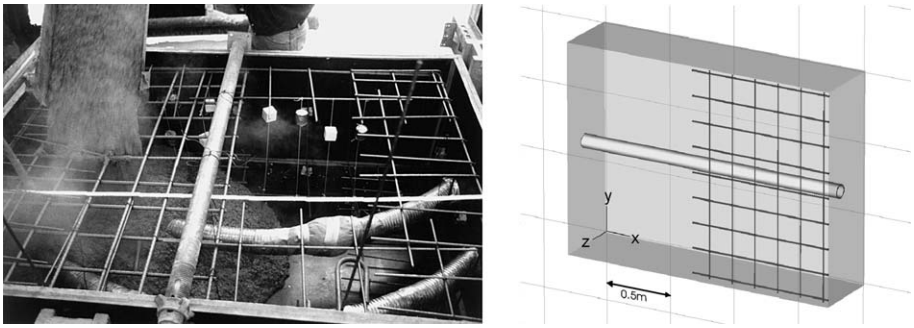

Fig. 1. (Left) Making of a test specimen: tendon duct below reinforcement embedded in concrete. (Right) Respective computer model of a test specimen for electromagnetic wave simulations.

given sources: electric and (fictitious) magnetic current densities $\underline{\mathbf{J}}_e(\underline{\mathbf{R}},t)$, $\underline{\mathbf{J}}_m(\underline{\mathbf{R}},t)$ whose pertinent charge densities $\varrho_e(\underline{\mathbf{R}},t)$, $\varrho_m(\underline{\mathbf{R}},t)$ define the source densities of the fluxes in terms of the scalar (dot) product with ∇.

2.1.2. Elastic waves

In solids, given (vector) force densities $\underline{\mathbf{f}}(\underline{\mathbf{R}},t)$ and (symmetric second rank tensor) deformation rate densities $\underline{\underline{\mathbf{h}}}(\underline{\mathbf{R}},t)$ act as sources of elastic waves, which are characterized by the field quantities: $\underline{\mathbf{j}}(\underline{\mathbf{R}},t)$ (vector momentum density), $\underline{\underline{\mathbf{T}}}(\underline{\mathbf{R}},t)$ (symmetric second rank stress tensor), $\underline{\underline{\mathbf{S}}}(\underline{\mathbf{R}},t)$ (symmetric second rank deformation tensor) and $\underline{\mathbf{v}}(\underline{\mathbf{R}},t)$ (vector particle velocity). Within a linearized theory of elasticity [1] these waves are governed by Newton–Cauchy's law of momentum conservation as well as the definition of the deformation rate through the symmetric part of the gradient dyadic $\nabla\underline{\mathbf{v}}(\underline{\mathbf{R}},t)$ ($\underline{\underline{\underline{\underline{\mathbf{I}}}}}^{+}$ denoting the fourth rank symmetrization tensor acting on $\nabla\underline{\mathbf{v}}$ by a double contraction ":")

$$\frac{\partial\underline{\mathbf{j}}(\underline{\mathbf{R}},t)}{\partial t} = \nabla\cdot\underline{\underline{\mathbf{T}}}(\underline{\mathbf{R}},t) + \underline{\mathbf{f}}(\underline{\mathbf{R}},t), \tag{2.5}$$

$$\frac{\partial\underline{\underline{\mathbf{S}}}(\underline{\mathbf{R}},t)}{\partial t} = \underline{\underline{\underline{\underline{\mathbf{I}}}}}^{+} : \nabla\underline{\mathbf{v}}(\underline{\mathbf{R}},t) + \underline{\underline{\mathbf{h}}}(\underline{\mathbf{R}},t). \tag{2.6}$$

2.1.3. Acoustic waves

In case of isotropic stresses being characterized by a scalar pressure $p(\underline{\mathbf{R}},t)$ through $\underline{\underline{\mathbf{T}}}(\underline{\mathbf{R}},t) = -p(\underline{\mathbf{R}},t)\underline{\underline{\mathbf{I}}}$—$\underline{\underline{\mathbf{I}}}$ denoting the second rank unit-tensor—the governing Eqs. (2.5) and (2.6) of elastodynamics reduce to the governing equations of (linear) acoustics:

$$\frac{\partial\underline{\mathbf{j}}(\underline{\mathbf{R}},t)}{\partial t} = -\nabla p(\underline{\mathbf{R}},t) + \underline{\mathbf{f}}(\underline{\mathbf{R}},t), \tag{2.7}$$

$$\frac{\partial S(\underline{\mathbf{R}},t)}{\partial t} = \nabla\cdot\underline{\mathbf{v}}(\underline{\mathbf{R}},t) + h(\underline{\mathbf{R}},t), \tag{2.8}$$

the second equation resulting from the trace of (2.6) with $S(\underline{\mathbf{R}},t) = \operatorname{trace}\underline{\underline{\mathbf{S}}}(\underline{\mathbf{R}},t)$, $h(\underline{\mathbf{R}},t) = \operatorname{trace}\underline{\underline{\mathbf{h}}}(\underline{\mathbf{R}},t)$, thus defining the dilatation $S(\underline{\mathbf{R}},t)$.

The formal comparison of the three systems of equations governing the propagation of wave fields exhibits a considerable similarity: First-order time derivatives of fields are related to combinations of first-order spatial derivatives in terms of curl, gradient and divergence, whence the particular spatial structure and polarization of the respective wave fields originate from. Yet the similarity gives rise to a unified treatment of forward propagation modeling and algorithmic inverse scattering, the two challenges to be met in nondestructive testing of concrete. Before entering this subject of modeling and inversion the three systems have to be complemented by constitutive equations relating field quantities in such a way that Eqs. (2.1) and (2.2), (2.5) and (2.6), (2.7) and (2.8) can be combined to derive explicit wave equations.

2.2. Constitutive equations

Constitutive equations do not follow from the governing equations by mere calculus, they have to be based on the physics of matter without violating the governing equations and their immediate consequences like conservation of momentum and energy together with physical principles like causality [1,2]. In the present context we concentrate on the simplest version of constitutive relations implying linearity, time invariance, instantaneous and local reaction as well as isotropy.

For electromagnetic wave fields this limitation defines the—inhomogeneous—permittivity $\epsilon_r(\underline{\mathbf{R}})$ and the permeability $\mu_r(\underline{\mathbf{R}})$:

$$\underline{\mathbf{D}}(\underline{\mathbf{R}},t) = \epsilon_0\epsilon_r(\underline{\mathbf{R}})\underline{\mathbf{E}}(\underline{\mathbf{R}},t), \tag{2.9}$$

$$\underline{\mathbf{B}}(\underline{\mathbf{R}},t) = \mu_0\mu_r(\underline{\mathbf{R}})\underline{\mathbf{H}}(\underline{\mathbf{R}},t), \tag{2.10}$$

where ϵ_0 and μ_0 denote the electric and magnetic field constants (in contrast to acousto-elastic waves electromagnetic waves travel through vacuum with $\epsilon_r(\underline{\mathbf{R}}) = 1, \mu_r(\underline{\mathbf{R}}) = 1$).

For elastic and acoustic waves the momentum density is simply related to the particle velocity through the mass density $\rho(\underline{\mathbf{R}})$:

$$\underline{\mathbf{j}}(\underline{\mathbf{R}},t) = \rho(\underline{\mathbf{R}})\underline{\mathbf{v}}(\underline{\mathbf{R}},t). \tag{2.11}$$

In case the material does not sustain shear stresses the acoustic approximation (2.7), (2.8) holds, and the relation between pressure and dilatation introduces the (adiabatic) compressibility $\kappa(\underline{\mathbf{R}})$:

$$S(\underline{\mathbf{R}},t) = -\kappa(\underline{\mathbf{R}})p(\underline{\mathbf{R}},t). \tag{2.12}$$

Of course, in the more general case of linear elasticity a relation between $\underline{\mathbf{T}}(\underline{\mathbf{R}},t)$ and $\underline{\mathbf{S}}(\underline{\mathbf{R}},t)$ has to be established which comes as the Cauchy–Hooke law

$$\underline{\mathbf{S}}(\underline{\mathbf{R}},t)=\underline{\underline{\underline{\underline{\mathbf{s}}}}}(\underline{\mathbf{R}}):\underline{\mathbf{T}}(\underline{\mathbf{R}},t) \tag{2.13}$$

introducing the compliance tensor $\underline{\underline{\underline{\underline{\mathbf{s}}}}}(\underline{\mathbf{R}})$ of rank four. Due to the symmetry of $\underline{\mathbf{S}}$ and $\underline{\mathbf{T}}$ (by virtue of definition and angular momentum conservation) and as a consequence of energy conservation the compliance tensor (for instantaneously reacting materials) has at most 21 independent entries (out of the original 81). A further reduction to only two parameters—the Lam constants $\lambda(\underline{\mathbf{R}})$ and $\mu(\underline{\mathbf{R}})$—is observed for isotropic materials yielding the representation

$$\underline{\underline{\underline{\underline{\mathbf{c}}}}}(\underline{\mathbf{R}})=\lambda(\underline{\mathbf{R}})\underline{\underline{\mathbf{I}}}\,\underline{\underline{\mathbf{I}}}+2\mu(\underline{\mathbf{R}})\underline{\underline{\underline{\underline{\mathbf{I}}}}}^{+} \tag{2.14}$$

for the stiffness tensor as the inverse of the compliance tensor ($\underline{\underline{\underline{\underline{\mathbf{s}}}}}:\underline{\underline{\underline{\underline{\mathbf{c}}}}}=\underline{\underline{\underline{\underline{\mathbf{c}}}}}:\underline{\underline{\underline{\underline{\mathbf{s}}}}}=\underline{\underline{\underline{\underline{\mathbf{I}}}}}^{+}$).

2.3. Fundamental solutions of wave equations

2.3.1. Wave equations for homogeneous materials

Accepting (2.11) and (2.12) for *homogeneous* materials—no $\underline{\mathbf{R}}$-dependence of ρ and κ—the simplest, while scalar, wave equation is obtained for the scalar pressure of acoustic waves if we take another time derivative of (2.8) and insert (2.7):

$$\begin{aligned}&\nabla\cdot\nabla p(\underline{\mathbf{R}},t)-\rho\kappa\frac{\partial^2 p(\underline{\mathbf{R}},t)}{\partial t^2}\\&\quad=\nabla\cdot\underline{\mathbf{f}}(\underline{\mathbf{R}},t)+\rho\frac{\partial h(\underline{\mathbf{R}},t)}{\partial t}.\end{aligned} \tag{2.15}$$

Starting in the way with (2.7) and inserting (2.8) results in

$$\nabla\nabla\cdot\underline{\mathbf{v}}(\underline{\mathbf{R}},t)-\rho\kappa\frac{\partial^2\underline{\mathbf{v}}(\underline{\mathbf{R}},t)}{\partial t^2}=-\kappa\frac{\partial\underline{\mathbf{f}}(\underline{\mathbf{R}},t)}{\partial t}-\nabla h(\underline{\mathbf{R}},t). \tag{2.16}$$

Notice: $\nabla\cdot\nabla=\Delta$ is the Laplace operator, and $\nabla\nabla$ is a dyadic product of the del-operator with itself.

For electromagnetic waves a similar procedure yields

$$\begin{aligned}&\nabla\times\nabla\times\underline{\mathbf{E}}(\underline{\mathbf{R}},t)+\epsilon_0\epsilon_r\mu_0\mu_r\frac{\partial^2\underline{\mathbf{E}}(\underline{\mathbf{R}},t)}{\partial t^2}\\&\quad=-\mu_0\mu_r\frac{\partial\underline{\mathbf{J}}_{\mathrm{e}}(\underline{\mathbf{R}},t)}{\partial t}-\nabla\times\underline{\mathbf{J}}_{\mathrm{m}}(\underline{\mathbf{R}},t).\end{aligned} \tag{2.17}$$

Finally, for elastic waves, Eq. (2.16) has to be augmented by a double-curl shear term:

$$\begin{aligned}&(\lambda+2\mu)\nabla\nabla\cdot\underline{\mathbf{v}}(\underline{\mathbf{R}},t)-\mu\nabla\times\nabla\times\underline{\mathbf{v}}(\underline{\mathbf{R}},t)\\&\quad-\rho\frac{\partial^2\underline{\mathbf{v}}(\underline{\mathbf{R}},t)}{\partial t^2}=-\frac{\partial\underline{\mathbf{f}}(\underline{\mathbf{R}},t)}{\partial t}-\nabla\cdot\underline{\underline{\underline{\underline{\mathbf{c}}}}}:\underline{\underline{\underline{\underline{\mathbf{h}}}}}(\underline{\mathbf{R}},t).\end{aligned} \tag{2.18}$$

2.3.2. Plane wave solutions of the homogeneous wave equations

With no sources present the resulting homogeneous wave equations have—among others—plane wave solutions. The acoustic plane pressure wave emanating from (2.15) reads

$$p(\underline{\mathbf{R}},t)=p_0\left(t-\frac{\hat{\underline{\mathbf{k}}}\cdot\underline{\mathbf{R}}}{c}\right). \tag{2.19}$$

Here, $c=\frac{1}{\sqrt{\rho\kappa}}$ denotes the (phase) wave speed, and $p_0(t)$ is an arbitrary time function. The plane wave has constant amplitude and phase in all planes perpendicular to the propagation direction given by the unit-vector $\hat{\underline{\mathbf{k}}}$. From the computation of the gradient in (2.7) we conclude that the pertinent vector $\underline{\mathbf{v}}(\underline{\mathbf{R}},t)$ has the direction of $\hat{\underline{\mathbf{k}}}$, which identifies a plane acoustic wave as being longitudinally polarized in the particle velocity. The mathematical origin is the appearance of the $\nabla\nabla$-operator in (2.16).

In contrast, plane electromagnetic waves are transverse waves, which goes back to the double curl-operator in (2.17). As plane wave solution of (2.17) we obtain

$$\underline{\mathbf{E}}(\underline{\mathbf{R}},t)=E_0\left(t-\frac{\hat{\underline{\mathbf{k}}}\cdot\underline{\mathbf{R}}}{c}\right)\hat{\underline{\mathbf{E}}}_0 \tag{2.20}$$

with the polarization vector $\hat{\underline{\mathbf{E}}}_0$ being orthogonal to $\hat{\underline{\mathbf{k}}}$ because $\hat{\underline{\mathbf{k}}}\cdot\hat{\underline{\mathbf{E}}}_0=0$ originating from the zero divergence of $\underline{\mathbf{E}}(\underline{\mathbf{R}},t)$ in free space; again, $E_0(t)$ is an arbitrary time function, which propagates through time and space with the (phase) velocity $c=\frac{1}{\sqrt{\epsilon_0\epsilon_r\mu_0\mu_r}}$.

The plane wave particle velocity of elastic waves as solution of the homogeneous Eq. (2.18) is calculated according to

$$\underline{\mathbf{v}}(\underline{\mathbf{R}},t)=v_{\mathrm{P}}\left(t-\frac{\hat{\underline{\mathbf{k}}}_{\mathrm{P}}\cdot\underline{\mathbf{R}}}{c_{\mathrm{P}}}\right)\hat{\underline{\mathbf{k}}}_{\mathrm{P}}+v_{\mathrm{S}}\left(t-\frac{\hat{\underline{\mathbf{k}}}_{\mathrm{S}}\cdot\underline{\mathbf{R}}}{c_{\mathrm{S}}}\right)\hat{\underline{\mathbf{v}}}_{\mathrm{S}} \tag{2.21}$$

with $\hat{\underline{\mathbf{k}}}_{\mathrm{S}}\cdot\hat{\underline{\mathbf{v}}}_{\mathrm{S}}=0$. On behalf of the simultaneous appearance of the $\nabla\nabla$- as well as the double curl-operator we anticipate the simultaneous existence of longitudinal—$\underline{\mathbf{v}}(\underline{\mathbf{R}},t)\times\hat{\underline{\mathbf{k}}}_{\mathrm{P}}=\underline{\mathbf{0}}$—as well as transverse waves—$\underline{\mathbf{v}}(\underline{\mathbf{R}},t)\cdot\hat{\underline{\mathbf{k}}}_{\mathrm{S}}=0$—with different wave speeds due to the different prefactors of the two operators in (2.18). As a matter of fact, the phase velocity of longitudinal waves appears as $c_{\mathrm{P}}=\sqrt{\frac{\lambda+2\mu}{\rho}}$ whereas the transverse waves travel with phase velocity $c_{\mathrm{S}}=\sqrt{\frac{\mu}{\rho}}$. Since $c_{\mathrm{P}}>c_{\mathrm{S}}$ the subscript P stands for primary and S for secondary waves indicating the earlier arrival time of P-waves against S-waves. Interesting enough, the subscripts also recognize the physical nature of P- and S-waves: P-waves are curl-free pressure waves and S-waves are purely solenoidal shear waves. In (2.21) $v_{\mathrm{P}}(t)$ and $v_{\mathrm{S}}(t)$ as well as $\hat{\underline{\mathbf{k}}}_{\mathrm{P}}$ and $\hat{\underline{\mathbf{k}}}_{\mathrm{S}}$ can be independently and arbitrarily chosen.

2.3.3. Spherical wave solutions of the inhomogeneous wave equations: Point source superposition

2.3.3.1. Acoustic waves. It is convenient to eliminate the time derivatives in the wave equations by means of a Fourier transform:

$$F(\omega)=\mathscr{F}\{f(t)\}=\int_{-\infty}^{\infty}f(t)\,\mathrm{e}^{\mathrm{j}\omega t}\,\mathrm{d}\omega; \tag{2.22}$$

$f(t)$ is a widely arbitrary time function, the variable ω denotes circular frequency and $j=\sqrt{-1}$; $F(\omega)$ is called the (often complex valued) spectrum of $f(t)$. The inverse of (2.22) turns out to be

$$f(t)=\mathscr{F}^{-1}\{F(\omega)\}=\frac{1}{2\pi}\int_{-\infty}^{\infty}F(\omega)\ \mathrm{e}^{-\mathrm{j}\omega t}\ \mathrm{d}\omega. \tag{2.23}$$

Taking the Fourier transforms of $p(\underline{\mathbf{R}},t)$, $\underline{\mathbf{f}}(\underline{\mathbf{R}},t)$ and $h(\underline{\mathbf{R}},t)$ with respect to time, the wave Eq. (2.15) transforms into the Helmholtz equation

$$\nabla\cdot\nabla p(\underline{\mathbf{R}},\omega)+k^2p(\underline{\mathbf{R}},\omega)=\nabla\cdot\underline{\mathbf{f}}(\underline{\mathbf{R}},\omega)-\mathrm{j}\omega\rho h(\underline{\mathbf{R}},\omega), \tag{2.24}$$

because $\mathscr{F}\left\{\frac{\partial f(t)}{\partial t}\right\}=-\mathrm{j}\omega F(\omega)$. In (2.24) we have introduced the wave number $k=\frac{\omega}{c}$.

The solution of the Helmholtz equation with given source spectra $\underline{\mathbf{f}}(\underline{\mathbf{R}},\omega)$ and $h(\underline{\mathbf{R}},\omega)$ is readily at hand if a specialized source, a point source at source point $\underline{\mathbf{R}}'$ represented by a three-dimensional delta-function $\delta(\underline{\mathbf{R}}-\underline{\mathbf{R}}')$, is considered first. The accordingly specialized Helmholtz equation

$$\nabla\cdot\nabla p(\underline{\mathbf{R}},\omega)+k^2p(\underline{\mathbf{R}},\omega)=-\delta(\underline{\mathbf{R}}-\underline{\mathbf{R}}') \tag{2.25}$$

defines the three-dimensional scalar Green function (spectrum)

$$p(\underline{\mathbf{R}},\omega)\Rightarrow G(\underline{\mathbf{R}}-\underline{\mathbf{R}}',\omega)=\frac{\mathrm{e}^{\mathrm{j}k|\underline{\mathbf{R}}-\underline{\mathbf{R}}'|}}{4\pi|\underline{\mathbf{R}}-\underline{\mathbf{R}}'|}, \tag{2.26}$$

which, when transformed back to the time domain by an inverse Fourier transform according to

$$G(\underline{\mathbf{R}}-\underline{\mathbf{R}}',t)=\frac{\delta\left(t-\frac{|\underline{\mathbf{R}}-\underline{\mathbf{R}}'|}{c}\right)}{4\pi|\underline{\mathbf{R}}-\underline{\mathbf{R}}'|}, \tag{2.27}$$

can be interpreted as a spherical wave with time dependence $\delta(t)$ emanating from the source point $\underline{\mathbf{R}}'$. Utilizing the Green function (2.26) the solution of (2.24) reads

$$p(\underline{\mathbf{R}},\omega)=\int\int\int_{V_Q}[\mathrm{j}\omega\rho h(\underline{\mathbf{R}}',\omega)-\nabla\cdot\underline{\mathbf{f}}(\underline{\mathbf{R}}',\omega)]\times G(\underline{\mathbf{R}}-\underline{\mathbf{R}}',\omega)\ \mathrm{d}^3\underline{\mathbf{R}}', \tag{2.28}$$

where it is understood that the given sources reside in a finite source volume V_Q embedded in a $\rho\kappa$-material being zero outside V_Q. Applying partial integration utilizing Gauss' theorem the volume integral (2.28) can be transformed into

$$p(\underline{\mathbf{R}},\omega)=\int\int\int_{V_Q}[\mathrm{j}\omega\rho h(\underline{\mathbf{R}}',\omega)G(\underline{\mathbf{R}}-\underline{\mathbf{R}}',\omega)+\underline{\mathbf{f}}(\underline{\mathbf{R}}',\omega)\cdot\nabla' G(\underline{\mathbf{R}}-\underline{\mathbf{R}}',\omega)]\ \mathrm{d}^3\underline{\mathbf{R}}' \tag{2.29}$$

thus exhibiting the source $\underline{\mathbf{f}}(\underline{\mathbf{R}},\omega)$ explicitly; $\nabla' G(\underline{\mathbf{R}}-\underline{\mathbf{R}}',\omega)$ denotes the gradient with respect to the source point coordinates. This integral representation is intuitively interpreted as a superposition of isotropic spherical waves emanating from source points within $h(\underline{\mathbf{R}}',\omega)$ and dipole waves with directionally dependent amplitudes emanating from source points within $\underline{\mathbf{f}}(\underline{\mathbf{R}}',\omega)$, it is a weighted point source superposition. In our context of nondestructive testing it is a mathematical representation of an incident (acoustic) wave field coming from given sources, i.e., it is a "transducer field".

For reasons to be obvious below we start to discuss mathematical representations of incident *acoustic* wave fields first.

2.3.3.2. Electromagnetic waves. Evaluation of the double curl operator in (2.17) and taking the Fourier transform with regard to time of $\underline{\mathbf{E}}(\underline{\mathbf{R}},t)$, $\underline{\mathbf{J}}_{\mathrm{e}}(\underline{\mathbf{R}},t)$ and $\underline{\mathbf{J}}_{\mathrm{m}}(\underline{\mathbf{R}},t)$ results in

$$\left[(\nabla\cdot\nabla+k^2)\underline{\underline{\mathbf{I}}}-\nabla\nabla\right]\cdot\underline{\mathbf{E}}(\underline{\mathbf{R}},\omega)=-\mathrm{j}\omega\mu_0\mu_r\underline{\mathbf{J}}_{\mathrm{e}}(\underline{\mathbf{R}},\omega)+\nabla\times\underline{\mathbf{J}}_{\mathrm{m}}(\underline{\mathbf{R}},\omega) \tag{2.30}$$

yielding a dyadic differential operator, which, when inverted, transforms into an integration with a dyadic Green function being defined by the differential equation

$$\left[(\nabla\cdot\nabla+k^2)\underline{\underline{\mathbf{I}}}-\nabla\nabla\right]\cdot\underline{\underline{\mathbf{G}}}(\underline{\mathbf{R}}-\underline{\mathbf{R}}',\omega)=-\underline{\underline{\mathbf{I}}}\delta(\underline{\mathbf{R}}-\underline{\mathbf{R}}'). \tag{2.31}$$

Its solution must certainly account for the "scalar wave operator" $\nabla\cdot\nabla+k^2$ (compare (2.24)) plus an additional term related to the $\nabla\nabla$-operator; as a result, the scalar Green function (2.26) appears explicitly augmented by a $\nabla\nabla$-term operating on this scalar Green function:

$$\underline{\underline{\mathbf{G}}}(\underline{\mathbf{R}}-\underline{\mathbf{R}}',\omega)=\left(\underline{\underline{\mathbf{I}}}+\frac{1}{k^2}\nabla'\nabla'\right)\frac{\mathrm{e}^{\mathrm{j}k|\underline{\mathbf{R}}-\underline{\mathbf{R}}'|}}{4\pi|\underline{\mathbf{R}}-\underline{\mathbf{R}}'|}. \tag{2.32}$$

Consequently, the electric field strength spectrum has the following point source superposition representation

$$\underline{\mathbf{E}}(\underline{\mathbf{R}},\omega)=\int\int\int_{V_Q}\left[\mathrm{j}\omega\mu_0\mu_r\underline{\mathbf{J}}_{\mathrm{e}}(\underline{\mathbf{R}}',\omega)\cdot\underline{\underline{\mathbf{G}}}(\underline{\mathbf{R}}-\underline{\mathbf{R}}',\omega)-\underline{\mathbf{J}}_{\mathrm{m}}(\underline{\mathbf{R}}',\omega)\cdot\nabla'\times\underline{\underline{\mathbf{G}}}(\underline{\mathbf{R}}-\underline{\mathbf{R}}',\omega)\right]\mathrm{d}^3\underline{\mathbf{R}}' \tag{2.33}$$

once the curl-operator on $\underline{\mathbf{J}}_{\mathrm{m}}$ in (2.30) has been shifted to the Green dyadic via Gauss' theorem.

In contrast to the scalar case (2.29) the amplitudes of *all* elementary spherical waves emanating from the source points $\underline{\mathbf{R}}'$ are now directionally dependent and, in addition, due to their dyadic structure a rotation between $\underline{\mathbf{J}}_{\mathrm{e}}(\underline{\mathbf{R}}',\omega)$, $\underline{\mathbf{J}}_{\mathrm{m}}(\underline{\mathbf{R}}',\omega)$ and $\underline{\mathbf{E}}(\underline{\mathbf{R}},\omega)$ is involved.

2.3.3.3. Elastic waves. The search for the Green function (tensor) of elastodynamics must simultaneously account for elementary P- and S-waves, which are "hidden" in the $(\nabla\nabla\cdot\underline{\mathbf{v}})$- and the $(\nabla\times\nabla\times\underline{\mathbf{v}})$-operators; we know from the plane wave solution that $\nabla\nabla\cdot\underline{\mathbf{v}}$ yields longitudinal primary (pressure) and that $\nabla\times\nabla\times\underline{\mathbf{v}}$ yields transverse secondary (shear) waves. From the electromagnetic case we learn to evaluate the double curl-operator into the two terms appearing in (2.30) with $k\Rightarrow k_{\mathrm{S}}$ whence an S-term similar to (2.32) should originate. It is therefore rather intuitive, that the following Green dyadic of elastodynamics

$$\underline{\underline{\Gamma}}(\underline{\mathbf{R}}-\underline{\mathbf{R}}',\omega)=-\frac{1}{\lambda+2\mu}\frac{1}{k_{\mathrm{P}}^2}\nabla'\nabla'\frac{\mathrm{e}^{\mathrm{j}k_{\mathrm{P}}|\underline{\mathbf{R}}-\underline{\mathbf{R}}'|}}{4\pi|\underline{\mathbf{R}}-\underline{\mathbf{R}}'|}+\frac{1}{\mu}\left(\underline{\underline{\mathbf{I}}}+\frac{1}{k_{\mathrm{S}}^2}\nabla'\nabla'\right)\frac{\mathrm{e}^{\mathrm{j}k_{\mathrm{S}}|\underline{\mathbf{R}}-\underline{\mathbf{R}}'|}}{4\pi|\underline{\mathbf{R}}-\underline{\mathbf{R}}'|} \tag{2.34}$$

is computed as a solution of

$$\left\{\mu\left[(\nabla\cdot\nabla+k_{\mathrm{S}}^2)\underline{\underline{\mathbf{I}}}-\nabla\nabla\right]+(\lambda+2\mu)\nabla\nabla\right\}\cdot\underline{\underline{\Gamma}}(\underline{\mathbf{R}}-\underline{\mathbf{R}}',\omega)=-\underline{\underline{\mathbf{I}}}\delta(\underline{\mathbf{R}}-\underline{\mathbf{R}}'). \tag{2.35}$$

It is indeed split into a spherical S- and a spherical P-wave term. The point source superposition representation of an incident elastic wave field coming from sources $\underline{\mathbf{f}}(\underline{\mathbf{R}},\omega)$ and $\underline{\underline{\mathbf{h}}}(\underline{\mathbf{R}},\omega)$ is therefore obtained as

$$\underline{\mathbf{v}}(\underline{\mathbf{R}},\omega)=\int\int\int_{V_Q}\left[-\mathrm{j}\omega\underline{\mathbf{f}}(\underline{\mathbf{R}}',\omega)\cdot\underline{\underline{\Gamma}}(\underline{\mathbf{R}}-\underline{\mathbf{R}}',\omega)-\underline{\underline{\mathbf{h}}}(\underline{\mathbf{R}}',\omega):\underline{\underline{\underline{\mathbf{c}}}}:\nabla'\underline{\underline{\Gamma}}(\underline{\mathbf{R}}-\underline{\mathbf{R}}',\omega)\right]\mathrm{d}^3\underline{\mathbf{R}}'. \tag{2.36}$$

For isotropic materials with $\underline{\underline{\underline{\mathbf{c}}}}$ according to (2.14) the term $\underline{\underline{\underline{\mathbf{c}}}}:\nabla'\underline{\underline{\Gamma}}$ can be further evaluated.

2.3.4. Acoustic wave equation for inhomogeneous materials

Tendon ducts with or without grouting defects are (strong) inhomogeneities in an embedding material (concrete) and as such they act as scatterers for an incident wave field: they are sources of a scattered field. As a matter of fact, in a mathematical representation of the scattered field, the scatterers can be replaced by equivalent or secondary sources (the sources of the incident field being considered as primary sources) representing their geometry and material composition, which enter the respective integrals of point source superposition. These integrals are subsequently bound for an inversion, i.e., to deduce the properties of the scatterer from the knowledge of the scattered (and incident) field. Recognizing the respective representations (2.29), (2.33) and (2.36) we perceive an increasing complexity from acoustic to electromagnetic and on to elastodynamic wave fields due to an increasing complexity of the underlying Green functions (dyadics). Therefore we start with the simplest case of acoustic waves when we derive explicit inversion schemes in order not to hide the principles behind the formalism.

Let us consider a material (of infinite extent) supporting acoustic waves having a (constant) mass density ρ and a (constant) compressibility κ; a scatterer of finite volume V_{c} with surface S_{c} is embedded in this material whose geometry is given by the characteristic function $\Gamma_{\mathrm{c}}(\underline{\mathbf{R}})$ of V_{c}:

$$\Gamma_{\mathrm{c}}(\underline{\mathbf{R}})=\begin{cases}0 & \text{for } \underline{\mathbf{R}}\notin V_{\mathrm{c}}\\ 1 & \text{for } \underline{\mathbf{R}}\in V_{\mathrm{c}}\end{cases}; \tag{2.37}$$

we assume that the mass density inside V_{c} is the same as outside, yet we admit an inhomogeneous compressibility $\kappa(\underline{\mathbf{R}})$ inside V_{c}. This scatterer is illuminated by an incident field coming from a finite source volume V_Q with only a non-zero dilatation rate $h(\underline{\mathbf{R}},t)$, i.e., we do not allow for a force density $\underline{\mathbf{f}}(\underline{\mathbf{R}},t)$. This situation is sketched in Fig. 2. In order to identify an inverse problem we need data: these should be the pressure $p(\underline{\mathbf{R}},t)$ on a (fictitious) surface S_M enclosing the volume V_M. The NDT-problem as an inverse scattering problem is then posed as follows: with the knowledge of the incident field and $p(\underline{\mathbf{R}},t)$ on S_M find the location of V_{c} and $\kappa(\underline{\mathbf{R}})$ within V_M, i.e., find the location, shape, size and character of a defect.

With the definition of the compressibility contrast

$$\chi_\kappa(\underline{\mathbf{R}})=\frac{1}{\kappa}[\kappa(\underline{\mathbf{R}})-\kappa]\Gamma_{\mathrm{c}}(\underline{\mathbf{R}}) \tag{2.38}$$

we can define an inhomogeneous compressibility

$$\kappa(\underline{\mathbf{R}}):=\kappa[1+\chi_\kappa(\underline{\mathbf{R}})]=\begin{cases}\kappa & \text{for } \underline{\mathbf{R}}\notin V_{\mathrm{c}}\\ \kappa(\underline{\mathbf{R}}) & \text{for } \underline{\mathbf{R}}\in V_{\mathrm{c}}\end{cases} \tag{2.39}$$

for *all* points in space inside and outside V_{c}. The Fourier-transformed governing Eqs. (2.7), (2.8) with (2.11) and (2.12) then read

$$-\mathrm{j}\omega\rho\underline{\mathbf{v}}(\underline{\mathbf{R}},\omega)=-\nabla p(\underline{\mathbf{R}},\omega), \tag{2.40}$$

$$\mathrm{j}\omega\kappa(\underline{\mathbf{R}})p(\underline{\mathbf{R}},\omega)=\nabla\cdot\underline{\mathbf{v}}(\underline{\mathbf{R}},\omega)+h(\underline{\mathbf{R}},\omega) \tag{2.41}$$

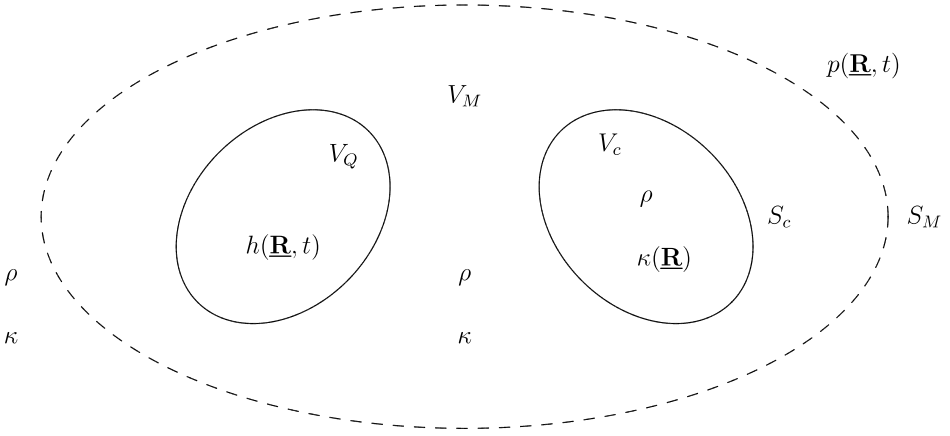

Fig. 2. NDT-Problem as an inverse scattering problem.

for $\underline{\mathbf{R}} \in \mathbb{R}^3$. Inserting (2.40) into (2.41) yields

$$\nabla \cdot \nabla p(\underline{\mathbf{R}},\omega) + \omega^2 \rho\kappa\, p(\underline{\mathbf{R}},\omega) = -\omega^2 \rho\kappa \chi_\kappa(\underline{\mathbf{R}}) p(\underline{\mathbf{R}},\omega) - \mathrm{j}\omega\rho h(\underline{\mathbf{R}},\omega) \tag{2.42}$$

identifying

$$h_\kappa(\underline{\mathbf{R}},\omega) = -\mathrm{j}\omega\kappa\chi_\kappa(\underline{\mathbf{R}}) p(\underline{\mathbf{R}},\omega) \tag{2.43}$$

as a secondary (dilatation rate) source, which is equivalent to the scatterer. By the way, an additional inhomogeneity of the mass density within V_c would result in an additional secondary force density source $\underline{\mathbf{f}}_\rho(\underline{\mathbf{R}},\omega) = \mathrm{j}\omega\rho\ \chi_\rho(\underline{\mathbf{R}})\underline{\mathbf{v}}(\underline{\mathbf{R}},\omega)$ containing the pertinent contrast $\chi_\rho(\underline{\mathbf{R}})$; its divergence would then additionally appear on the right-hand side of (2.43) thus complicating the inversion considerably.

3. Wave field inversion: Acoustic waves

3.1. Wave field inversion as a nonlinear problem

With the help of the Green function (2.26) the solution of (2.42) is readily obtained (compare (2.28)) in terms of the superposition $p(\underline{\mathbf{R}},\omega) = p_i(\underline{\mathbf{R}},\omega) + p_s(\underline{\mathbf{R}},\omega)$ of the incident field $p_i(\underline{\mathbf{R}},\omega)$ and the scattered field $p_s(\underline{\mathbf{R}},\omega)$:

$$p_i(\underline{\mathbf{R}},\omega) = \mathrm{j}\omega\rho \int\int\int_{V_Q} h(\underline{\mathbf{R}}',\omega) G(\underline{\mathbf{R}} - \underline{\mathbf{R}}',\omega)\mathrm{d}^3\underline{\mathbf{R}}', \tag{3.1}$$

$$p_s(\underline{\mathbf{R}},\omega) = k^2 \int\int\int_{V_c} \chi_\kappa(\underline{\mathbf{R}}') p(\underline{\mathbf{R}}',\omega) G(\underline{\mathbf{R}} - \underline{\mathbf{R}}',\omega)\mathrm{d}^3\underline{\mathbf{R}}'. \tag{3.2}$$

Since $p_s(\underline{\mathbf{R}} \in S_M,\omega)$ are the data, grabbing $\chi_\kappa(\underline{\mathbf{R}})$ is via inversion of (3.2)! Unfortunately, the *total* field $p(\underline{\mathbf{R}},\omega)$ is required under the integral implying the knowledge of the scattered field *inside* V_c, where, by definition, one has no access. Hence, without any further approximation the inverse scattering problem is a *nonlinear* problem, which is rather difficult to deal with; up to now, there is no algorithm really available for practical applications [3].

3.2. Linearization

The simplest way to linearize the inverse scattering problem is to replace $p(\underline{\mathbf{R}} \in V_c,\omega)$ by something known, i.e., the incident field alone. This comes as the Born approximation for weak scatterers, yet for strong scatterers, for instance voids in the $\rho\kappa$-material, the complementary Kirchhoff approximation can be dealt with along the same guidelines [4]. Even though rather stringent both approximations have proved extremely useful in nondestructive testing [5,6]. Therefore we start the derivation of inversion algorithms with the linearized representation

$$p_s^{\mathrm{Born}}(\underline{\mathbf{R}},\omega) = k^2 \int\int\int_{V_c} \chi_\kappa(\underline{\mathbf{R}}') p_i(\underline{\mathbf{R}}',\omega) G(\underline{\mathbf{R}} - \underline{\mathbf{R}}',\omega)\mathrm{d}^3\underline{\mathbf{R}}' \tag{3.3}$$

of the scattered field.

3.2.1. Multi-bistatic inversion: Frequency and angular diversity

Let us assume a plane wave as incident field; according to (2.19) its Fourier spectrum reads:

$$p_i(\underline{\mathbf{R}},\omega) = p_0(\omega)\mathrm{e}^{\mathrm{j}\underline{\mathbf{k}}_i\cdot\underline{\mathbf{R}}}; \tag{3.4}$$

the phase vector $\underline{\mathbf{k}}_i$ contains two parameters, i.e., (circular) frequency ω via $|\underline{\mathbf{k}}_i| = k = \frac{\omega}{c}$ and illumination angle via the propagation direction unit-vector $\hat{\underline{\mathbf{k}}}_i = \frac{\underline{\mathbf{k}}_i}{k}$, which stands for the transducer location. The receiver at location $\underline{\mathbf{R}}$ is supposed to scan the surface S_M. For *one* choice of $\hat{\underline{\mathbf{k}}}_i$ and *one* choice of $\underline{\mathbf{R}}$, radar people call this a bistatic set-up, NDT people call it a pitch-catch set-up. Consequently, if $\underline{\mathbf{R}}$ varies on S_M we face a multi-bistatic arrangement, which must reflect itself in an inversion algorithm. Therefore, we start with

$$p_s^{\mathrm{Born}}(\underline{\mathbf{R}},\omega,\hat{\underline{\mathbf{k}}}_i) = k^2 p_0(\omega) \int\int\int_{V_c} \chi_\kappa(\underline{\mathbf{R}}')\mathrm{e}^{\mathrm{j}\underline{\mathbf{k}}_i\cdot\underline{\mathbf{R}}'} \times \frac{\mathrm{e}^{\mathrm{j}k|\underline{\mathbf{R}}-\underline{\mathbf{R}}'|}}{4\pi|\underline{\mathbf{R}}-\underline{\mathbf{R}}'|}\mathrm{d}^3\underline{\mathbf{R}}'. \tag{3.5}$$

Recognizing the fact, that our NDT application mostly faces planar measurement surfaces S_M, say an xy-plane at distance $z = d$ from an appropriately chosen cartesian coordinate origin, we can express $|\underline{\mathbf{R}} - \underline{\mathbf{R}}'|$ as

$$|\underline{\mathbf{R}} - \underline{\mathbf{R}}'| = \sqrt{(x-x')^2 + (y-y')^2 + (d-z')^2}; \quad x,y \in S_M,\ x',y',z' \in V_M. \tag{3.6}$$

The choice of cartesian coordinates clearly identifies (3.5) as a two-dimensional convolution integral with regard to x' and y', which can be resolved applying the convolution theorem of the two-dimensional spatial Fourier transform

$$\hat{\phi}(K_x,K_y) = \int_{-\infty}^{\infty}\int_{-\infty}^{\infty} \phi(x,y)\mathrm{e}^{-\mathrm{j}K_x x - \mathrm{j}K_y y}\,\mathrm{d}x\mathrm{d}y = \mathscr{F}_{xy}\{\phi(x,y)\} \tag{3.7}$$

with the inverse transform

$$\phi(x,y) = \frac{1}{(2\pi)^2}\int_{-\infty}^{\infty}\int_{-\infty}^{\infty} \hat{\phi}(K_x,K_y)\mathrm{e}^{\mathrm{j}K_x x + \mathrm{j}K_y y}\,\mathrm{d}K_x\mathrm{d}K_y = \mathscr{F}^{-1}_{K_xK_y}\{\hat{\phi}(K_x,K_y)\}. \tag{3.8}$$

Notice: We have chosen the signs in the kernel exponentials opposite to (2.22) and (2.23). With the knowledge of the two-dimensional spatial Fourier spectrum

$$\widehat{G}(K_x,K_y,d-z',\omega) = \frac{\mathrm{j}}{2\sqrt{k^2-K_x^2-K_y^2}}\mathrm{e}^{\mathrm{j}|d-z'|\sqrt{k^2-K_x^2-K_y^2}} \tag{3.9}$$

of the scalar Green function we obtain

$$\hat{p}_s^{\mathrm{Born}}(K_x+k_{ix},K_y+k_{iy},d,\omega) = k^2 p_0(\omega)\frac{\mathrm{j}\mathrm{e}^{\mathrm{j}d\sqrt{k^2-(K_x+k_{ix})^2-(K_y+k_{iy})^2}}}{2\sqrt{k^2-(K_x+k_{ix})^2-(K_y+k_{iy})^2}} \times \int_{-\infty}^{\infty}\hat{\chi}_\kappa(K_x,K_y,z')\mathrm{e}^{-\mathrm{j}z'(\sqrt{k^2-(K_x+k_{ix})^2-(K_y+k_{iy})^2}-k_{iz})}\,\mathrm{d}z' \tag{3.10}$$

from Eq. (3.5) after multiplying it with $\mathrm{e}^{-\mathrm{j}\underline{\mathbf{k}}_i\cdot\underline{\mathbf{R}}}$ and assuming $d > z'$. After the definition of a third spatial Fourier variable K_z through

$$K_z = \sqrt{k^2-(K_x+k_{ix})^2-(K_y+k_{iy})^2}-k_{iz} \tag{3.11}$$

we identify the remaining z'-integral as another Fourier integral yielding the bistatic Fourier diffraction slice theorem

$$\hat{p}_s^{\mathrm{Born}}(K_x+k_{ix},K_y+k_{iy},d,\omega) = k^2 p_0(\omega)\frac{\mathrm{j}}{2(K_z+k_{iz})}\mathrm{e}^{\mathrm{j}d(K_z+k_{iz})}\tilde{\chi}_\kappa(K_x,K_y,K_z), \tag{3.12}$$

which relates the two-dimensional spatial Fourier transform of the data to the three-dimensional spatial Fourier transform of the κ-contrast (denoted by $\tilde{\chi}_\kappa$). Writing (3.11) in vector notation according to $|\underline{\mathbf{K}}+\underline{\mathbf{k}}_i| = k$ introducing the Fourier vector $\underline{\mathbf{K}}$, i.e., $\underline{\mathbf{K}}$-space, with the cartesian components K_x, K_y, K_z tells us that the Fourier transformed data have to be placed on a half sphere in $\underline{\mathbf{K}}$-space with midpoint $\underline{\mathbf{k}}_i$ and radius k (Fig. 3). In an impulsive illumination (with fixed $\hat{\underline{\mathbf{k}}}_i$) a frequency band is at hand and, hence, the radius of the sphere can be varied leading to a specific coverage of $\underline{\mathbf{K}}$-space in terms of frequency diversity, whereas a different coverage in terms of angular diversity is obtained for a fixed frequency varying the illumination direction $\hat{\underline{\mathbf{k}}}_i$. Of course, as soon as a particular coverage of $\underline{\mathbf{K}}$-space is completed, a three-dimensional inverse spatial Fourier transform yields a bandlimited version (due to the finite coverage of $\underline{\mathbf{K}}$-space) of the contrast function.

3.2.2. Multi-monostatic inversion: Frequency diversity

A common experimental set-up in NDT relies on the simultaneous scan of transmitting and receiving transducers; if they both collapse into only one device, a pulse–echo or, in radar terminology, a monostatic experiment is performed, and, when the device is scanned along a surface, it is a multi-monostatic experiment. In that case, the incident field is conveniently modeled by a point source at $\underline{\mathbf{R}}_0 \in S_M$:

$$p_i(\underline{\mathbf{R}},\omega,\underline{\mathbf{R}}_0) = p_0(\omega)\frac{\mathrm{e}^{\mathrm{j}k|\underline{\mathbf{R}}-\underline{\mathbf{R}}_0|}}{4\pi|\underline{\mathbf{R}}-\underline{\mathbf{R}}_0|}. \tag{3.13}$$

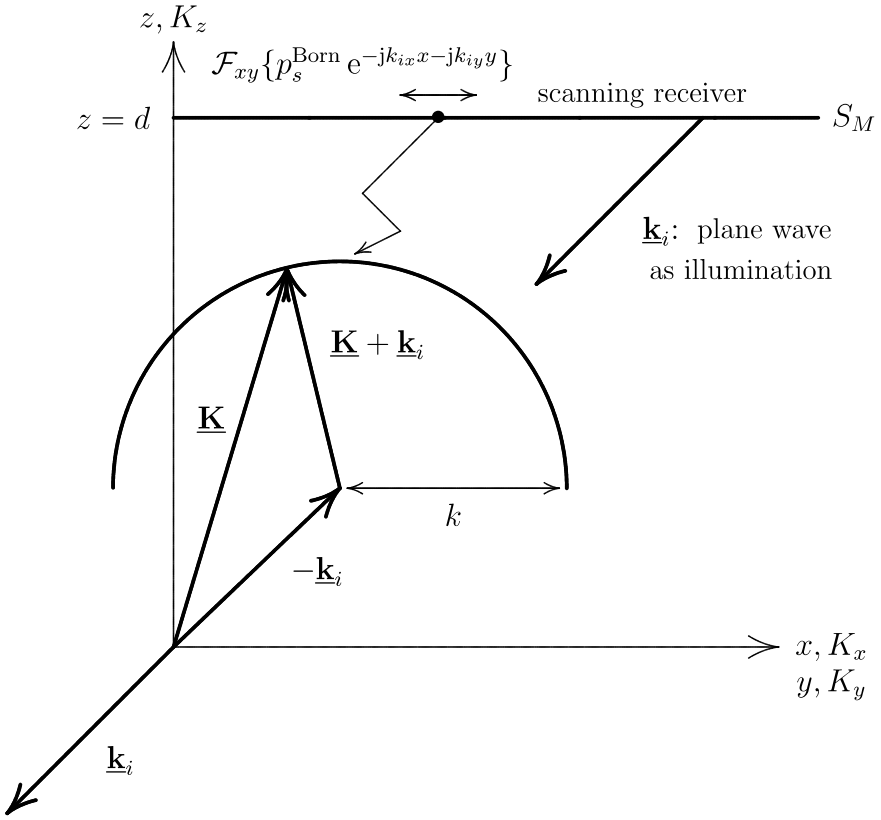

Fig. 3. Mapping spatially Fourier transformed multi-bistatic data into $\underline{\mathbf{K}}$-space.

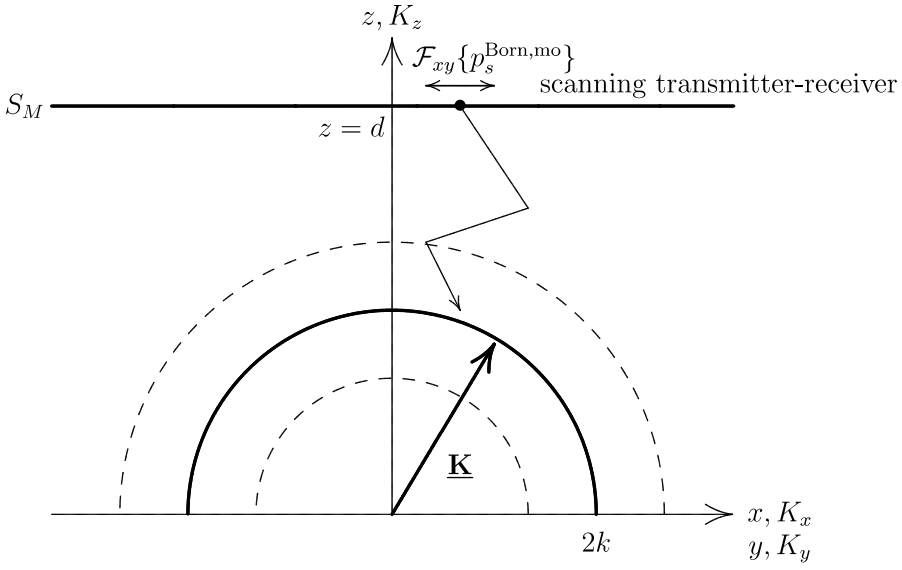

Fig. 4. Mapping spatially Fourier transformed multi-monostatic data into $\underline{\mathbf{K}}$-space.

Insertion into (3.5) yields $\underline{\mathbf{R}} \Rightarrow \underline{\mathbf{R}}'$, and the multi-monostatic set-up requires $\underline{\mathbf{R}} \Rightarrow \underline{\mathbf{R}}_0$ whence the following expression is obtained:

$$p_{\mathrm{s}}^{\mathrm{Born,m}}(\underline{\mathbf{R}},\omega) = k^2 p_0(\omega)\int_{-\infty}^{\infty}\int_{-\infty}^{\infty}\int_{-\infty}^{\infty}\chi(\underline{\mathbf{R}}') \times \frac{\mathrm{e}^{2\mathrm{j}k|\underline{\mathbf{R}}-\underline{\mathbf{R}}'|}}{(4\pi)^2|\underline{\mathbf{R}}-\underline{\mathbf{R}}'|^2}\mathrm{d}^3\underline{\mathbf{R}}'; \tag{3.14}$$

the upper index m stands for monostatic. Unfortunately, at that point, we cannot immediately proceed as before, because, due to the square in the denominator, the kernel of the integral is not a Green function, and, hence, its two-dimensional spatial Fourier transform is not known analytically. Yet the following definition

$$p_{\mathrm{s}}^{\mathrm{Born,mo}}(\underline{\mathbf{R}},\omega) = \frac{2\pi}{\mathrm{j}}\frac{\partial}{\partial k}\frac{p_{\mathrm{s}}^{\mathrm{Born,m}}(\underline{\mathbf{R}},\omega)}{k^2 p_0(\omega)} \tag{3.15}$$

of a modified (monostatic) field leads to

$$p_{\mathrm{s}}^{\mathrm{Born,mo}}(\underline{\mathbf{R}},\omega) = \int_{-\infty}^{\infty}\int_{-\infty}^{\infty}\int_{-\infty}^{\infty}\chi(\underline{\mathbf{R}}')\frac{\mathrm{e}^{2\mathrm{j}k|\underline{\mathbf{R}}-\underline{\mathbf{R}}'|}}{4\pi|\underline{\mathbf{R}}-\underline{\mathbf{R}}'|}\mathrm{d}^3\underline{\mathbf{R}}', \tag{3.16}$$

which contains a Green function with k replaced by $2k$. Obviously, applying Fourier transforms as before implying the definition of

$$K_z = \sqrt{4k^2 - K_x^2 - K_y^2} \geqslant 0 \Longleftrightarrow |\underline{\mathbf{K}}| = 2k \tag{3.17}$$

yields

$$\hat{p}_{\mathrm{s}}^{\mathrm{Born,mo}}(K_x,K_y,d,\omega) = \frac{\mathrm{j}}{2K_z}\mathrm{e}^{\mathrm{j}dK_z}\tilde{\chi}(K_x,K_y,K_z) \tag{3.18}$$

as the algorithm to map Fourier transformed multi-monostatic data into $\underline{\mathbf{K}}$-space. This time, the half spheres under concern are origin centered, and the coverage of a finite sub-set of $\underline{\mathbf{K}}$-space can only be achieved with a variation of frequency (frequency diversity). This is illustrated in Fig. 4.

3.3. Wave field inversion: Electromagnetic and elastic waves

3.3.1. Electromagnetic waves

3.3.1.1. Born linearization. In the acoustic case we simplified the inversion considering only a compressibility inhomogeneity in V_{c} thus avoiding having to deal with the gradient of the scalar Green function. In the electromagnetic case however we face at least the Green dyadic (2.32) exhibiting a dyadic del-operation on the scalar Green function; yet we can avoid an additional curl-operation disregarding magnetic current densities. This amounts to disregarding an inhomogeneity in the permeability keeping only an inhomogeneous permittivity $\epsilon_r(\underline{\mathbf{R}})$ in V_{c}. Such an inhomogeneity immediately yields the definition of an equivalent electric current density

$$\underline{\mathbf{J}}_{\mathrm{ec}}(\underline{\mathbf{R}},\omega) = -\mathrm{j}\omega\epsilon_0\epsilon_r\chi_{\mathrm{e}}(\underline{\mathbf{R}})\underline{\mathbf{E}}(\underline{\mathbf{R}},\omega) \tag{3.19}$$

quite similar to (2.43). Here, $\chi_{\mathrm{e}}(\underline{\mathbf{R}})$ according to

$$\chi_{\mathrm{e}}(\underline{\mathbf{R}}) = \frac{1}{\epsilon_r}[\epsilon_r(\underline{\mathbf{R}}) - \epsilon_r]\Gamma_{\mathrm{c}}(\underline{\mathbf{R}}) \tag{3.20}$$

defines the permittivity contrast function. Introducing the Born approximation with a plane wave incident field

$$\underline{\mathbf{E}}_i(\underline{\mathbf{R}},\omega) = E_0(\omega)\mathrm{e}^{\mathrm{j}\underline{\mathbf{k}}_i\cdot\underline{\mathbf{R}}}\widehat{\underline{\mathbf{E}}}_0 \tag{3.21}$$

the point source superposition representation of the scattered field is obtained from (2.33):

$$\underline{\mathbf{E}}_{\mathrm{s}}^{\mathrm{Born}}(\underline{\mathbf{R}},\omega,\hat{\underline{\mathbf{k}}}_i,\widehat{\underline{\mathbf{E}}}_0) = k^2 E_0(\omega)\widehat{\underline{\mathbf{E}}}_0 \cdot\int\int\int_{V_{\mathrm{c}}}\chi_{\mathrm{e}}(\underline{\mathbf{R}}')\mathrm{e}^{\mathrm{j}\underline{\mathbf{k}}_i\cdot\underline{\mathbf{R}}'}\left(\underline{\underline{\mathbf{I}}} + \frac{1}{k^2}\nabla'\nabla'\right)\frac{\mathrm{e}^{\mathrm{j}k|\underline{\mathbf{R}}-\underline{\mathbf{R}}'|}}{4\pi|\underline{\mathbf{R}}-\underline{\mathbf{R}}'|}\mathrm{d}^3\underline{\mathbf{R}}'. \tag{3.22}$$

Proceeding as in the acoustic case we derive the electromagnetic bistatic Fourier diffraction slice theorem

$$\widehat{\underline{\mathbf{E}}}_{\mathrm{s}}^{\mathrm{Born}}(K_x+k_{ix},K_y+k_{iy},d,\omega,k_{iz},\widehat{\underline{\mathbf{E}}}_0)$$
$$=k^2E_0(\omega)\frac{\mathrm{j}}{2(K_z+k_{iz})}\mathrm{e}^{\mathrm{j}d(K_z+k_{iz})}$$
$$\times\underbrace{\left[\underline{\underline{\mathbf{I}}}-\frac{1}{k^2}(\underline{\mathbf{K}}+\underline{\mathbf{k}}_i)(\underline{\mathbf{K}}+\underline{\mathbf{k}}_i)\right]}_{=\underline{\underline{\mathbf{W}}}(\underline{\mathbf{K}},\underline{\mathbf{k}}_i)}\cdot\widehat{\underline{\mathbf{E}}}_0\tilde{\chi}_{\mathrm{e}}(\underline{\mathbf{K}}) \tag{3.23}$$

as a vector counterpart of (3.12); the Fourier vector $\underline{\mathbf{K}}$ has cartesian components K_x, K_y, K_z with K_z given by (3.11), i.e., we have $|\underline{\mathbf{K}}+\underline{\mathbf{k}}_i|=k$. Resolving (3.23) for $\tilde{\chi}_{\mathrm{e}}(\underline{\mathbf{K}})$ involves the task of inverting the second rank tensor $\underline{\underline{\mathbf{W}}}(\underline{\mathbf{K}},\underline{\mathbf{k}}_i)$; since $\det\underline{\underline{\mathbf{W}}}(\underline{\mathbf{K}},\underline{\mathbf{k}}_i)=0$ [7], this is not possible, but recognizing $\underline{\mathbf{k}}_i\cdot\widehat{\underline{\mathbf{E}}}_0=0$, one basically faces the inversion of

$$\underline{\underline{\mathbf{w}}}(\underline{\mathbf{K}},\underline{\mathbf{k}}_i)=\underline{\underline{\mathbf{I}}}-\frac{1}{k^2}(\underline{\mathbf{K}}+\underline{\mathbf{k}}_i)\underline{\mathbf{K}} \tag{3.24}$$

yielding [7]

$$\widehat{\underline{\mathbf{E}}}_0\cdot\left[\underline{\underline{\mathbf{I}}}-\frac{(\underline{\mathbf{K}}+\underline{\mathbf{k}}_i)\underline{\mathbf{K}}}{(\underline{\mathbf{K}}+\underline{\mathbf{k}}_i)\cdot\underline{\mathbf{K}}-k^2}\right]\cdot\widehat{\underline{\mathbf{E}}}_{\mathrm{s}}^{\mathrm{Born}}(K_x+k_{ix},K_y+k_{iy},d,\omega,k_{iz},\widehat{\underline{\mathbf{E}}}_0)$$
$$=k^2E_0(\omega)\frac{\mathrm{j}}{2(K_z+k_{iz})}\mathrm{e}^{\mathrm{j}d(K_z+k_{iz})}\tilde{\chi}_{\mathrm{e}}(\underline{\mathbf{K}}). \tag{3.25}$$

The first term $\widehat{\underline{\mathbf{E}}}_0\cdot\widehat{\underline{\mathbf{E}}}^{\mathrm{Born}}$ on the left-hand side of (3.24) provides a *scalar* inversion scheme for electromagnetic vector waves whereas the second term can be understood as a polarimetric correction.

An alternative inversion formula is obtained if (3.23) is dot-multiplied with $\widehat{\underline{\mathbf{E}}}_0\cdot\underline{\underline{\mathbf{W}}}(\underline{\mathbf{K}},\underline{\mathbf{k}}_i)$ yielding

$$\widehat{\underline{\mathbf{E}}}_0\cdot\left[\underline{\underline{\mathbf{I}}}-\frac{1}{k^2}(\underline{\mathbf{K}}+\underline{\mathbf{k}}_i)(\underline{\mathbf{K}}+\underline{\mathbf{k}}_i)\right]$$
$$\cdot\widehat{\underline{\mathbf{E}}}_{\mathrm{s}}^{\mathrm{Born}}(K_x+k_{ix},K_y+k_{iy},d,\omega,k_{iz},\widehat{\underline{\mathbf{E}}}_0)$$
$$=k^2E_0(\omega)\frac{\mathrm{j}}{2(K_z+k_{iz})}\mathrm{e}^{\mathrm{j}d(K_z+k_{iz})}$$
$$\times\left\{\widehat{\underline{\mathbf{E}}}_0\cdot\left[\underline{\underline{\mathbf{I}}}-\frac{1}{k^2}(\underline{\mathbf{K}}+\underline{\mathbf{k}}_i)(\underline{\mathbf{K}}+\underline{\mathbf{k}}_i)\right]\right\}^2\tilde{\chi}_{\mathrm{e}}(\underline{\mathbf{K}}). \tag{3.26}$$

3.3.1.2. Kirchhoff linearization. In general, the surfaces of tendon ducts can be approximated by a perfect (infinite) electric conductivity yielding

$$\underline{\mathbf{J}}_{\mathrm{ec}}(\underline{\mathbf{R}},\omega)=\underline{\gamma}_c(\underline{\mathbf{R}})\times\underline{\mathbf{H}}(\underline{\mathbf{R}},\omega) \tag{3.27}$$

as an equivalent source; here, the vector singular function $\underline{\gamma}_{\mathrm{c}}(\underline{\mathbf{R}})=\underline{\mathbf{n}}\gamma_{\mathrm{c}}(\underline{\mathbf{R}})$ of the surface S_{c} has the direction of the (outward) normal unit-vector $\underline{\mathbf{n}}$, and the singular function $\gamma_{\mathrm{c}}(\underline{\mathbf{R}})$ has the distributional sifting property reducing a volume integral over V_{c} to a surface integral over S_{c}. In that sense, the current density $\underline{\mathbf{J}}_{\mathrm{ec}}(\underline{\mathbf{R}},\omega)$ is a *volume* current density. Calculation of $\underline{\gamma}_{\mathrm{c}}(\underline{\mathbf{R}})$ is in terms of $-\nabla\Gamma_{\mathrm{c}}(\underline{\mathbf{R}})$ resulting in $\nabla\times\underline{\gamma}_{\mathrm{c}}(\underline{\mathbf{R}})=\underline{\mathbf{0}}$ [8]. As it is true for all equivalent sources, the current density (3.27) depends upon the total (magnetic) field, linearization is in terms of the incident field $\underline{\mathbf{H}}_i(\underline{\mathbf{R}},\omega)$ resulting in the physical optics current density

$$\underline{\mathbf{J}}_{ec}^{\mathrm{PO}}(\underline{\mathbf{R}},\omega)=2\underline{\gamma}_u(\underline{\mathbf{R}})\times\underline{\mathbf{H}}_i(\underline{\mathbf{R}},\omega)$$
$$=E_0(\omega)2\sqrt{\frac{\epsilon_0\epsilon_r}{\mu_0\mu_r}}\underline{\gamma}_u(\underline{\mathbf{R}})\times\left(\hat{\underline{\mathbf{k}}}_i\times\widehat{\underline{\mathbf{E}}}_0\right)\mathrm{e}^{\mathrm{j}\underline{\mathbf{k}}_i\cdot\underline{\mathbf{R}}}$$
$$=E_0(\omega)$$
$$\times\underbrace{2\sqrt{\frac{\epsilon_0\epsilon_r}{\mu_0\mu_r}}\left[\hat{\underline{\mathbf{k}}}_i\underline{\gamma}_u(\underline{\mathbf{R}})\cdot\widehat{\underline{\mathbf{E}}}_0-\widehat{\underline{\mathbf{E}}}_0\underline{\gamma}_u(\underline{\mathbf{R}})\cdot\hat{\underline{\mathbf{k}}}_i\right]}_{=\underline{\mathbf{J}}_{\mathrm{c}}(\underline{\mathbf{R}})}\mathrm{e}^{\mathrm{j}\underline{\mathbf{k}}_i\cdot\underline{\mathbf{R}}} \tag{3.28}$$

according to the Kirchhoff approximation, introducing a sharp shadow boundary via a step-function $u(-\hat{\underline{\mathbf{k}}}_i\cdot\underline{\mathbf{n}})$, which is hidden as a factor in $\underline{\gamma}_u(\underline{\mathbf{R}})$ thus characterizing the illuminated part of the surface of the scatterer only; the Kirchhoff approximation holds for smooth convex scatterers (like tendon ducts).

Instead of (3.25) we obtain the inversion formula

$$\left[\underline{\underline{\mathbf{I}}}-\frac{(\underline{\mathbf{K}}+\underline{\mathbf{k}}_i)\underline{\mathbf{k}}_i}{\underline{\mathbf{K}}\cdot\underline{\mathbf{k}}_i}\right]$$
$$\cdot\widehat{\underline{\mathbf{E}}}_{\mathrm{s}}^{\mathrm{PO}}\left(K_x+k_{ix},K_y+k_{iy},d,\omega,k_{iz},\widehat{\underline{\mathbf{E}}}_0\right)$$
$$=\mathrm{j}\omega\mu_0\mu_rE_0(\omega)\frac{\mathrm{j}}{2(K_z+k_{iz})}\mathrm{e}^{\mathrm{j}d(K_z+k_{iz})}\widetilde{\underline{\mathbf{J}}}_{\mathrm{ec}}(\underline{\mathbf{K}}) \tag{3.29}$$

from which the components of $\widetilde{\underline{\gamma}}_u(\underline{\mathbf{K}})\cdot\widehat{\underline{\mathbf{E}}}_0$ and $\widetilde{\underline{\gamma}}_u(\underline{\mathbf{K}})\cdot\hat{\underline{\mathbf{k}}}_i$ can be recovered via dot-multiplication with $\hat{\underline{\mathbf{k}}}_i$ and $\widehat{\underline{\mathbf{E}}}_0$, respectively. A third component in an orthonormal set of unit-vectors $\hat{\underline{\mathbf{k}}}_i$, $\widehat{\underline{\mathbf{E}}}_0$, $\widehat{\underline{\mathbf{E}}}_{\mathrm{orth}}$ is obtained if a second experiment is performed with a polarization $\widehat{\underline{\mathbf{E}}}_{\mathrm{orth}}$ orthogonal to $\widehat{\underline{\mathbf{E}}}_0$, hence, in principle, the scattering surface can be recovered.

3.3.2. Elastic waves

Referring to the pertinent point-source representation (2.36) of the scattered field we can basically proceed as with electromagnetic waves. For the sake of simplicity we consider only a ρ-inhomogeneity which gives rise to an equivalent force density

$$\underline{\mathbf{f}}_{\rho}(\underline{\mathbf{R}},\omega)=-\mathrm{j}\omega\rho\chi_{\rho}(\underline{\mathbf{R}})\underline{\mathbf{v}}(\underline{\mathbf{R}},\omega) \tag{3.30}$$

involving the ρ-contrast function

$$\chi_{\rho}(\underline{\mathbf{R}})=\frac{1}{\rho}[\rho(\underline{\mathbf{R}})-\rho]\Gamma_{\mathrm{c}}(\underline{\mathbf{R}}) \tag{3.31}$$

in a manner similar to (2.38). The incident wave can be either a plane pressure or a plane shear wave

$$\underline{\mathbf{v}}_i^{\mathrm{P,S}}(\underline{\mathbf{R}},\omega)=v_{\mathrm{P,S}}(\omega)\mathrm{e}^{\mathrm{j}\underline{\mathbf{k}}_i^{\mathrm{P,S}}\cdot\underline{\mathbf{R}}}\hat{\underline{\mathbf{v}}}_{\mathrm{P,S}} \tag{3.32}$$

with phase vectors $\underline{\mathbf{k}}_i^{\mathrm{P,S}}=k_{\mathrm{P,S}}\hat{\underline{\mathbf{k}}}_i^{\mathrm{P,S}}$ and polarizations $\hat{\underline{\mathbf{v}}}_{\mathrm{P}}=\hat{\underline{\mathbf{k}}}_{\mathrm{P}}$ and $\hat{\underline{\mathbf{v}}}_{\mathrm{S}}\times\hat{\underline{\mathbf{k}}}_{\mathrm{S}}=\underline{\mathbf{0}}$. From (2.36) we obtain within the Born linearization

$$\underline{\mathbf{v}}_{\mathrm{s}}^{\mathrm{Born}}(\underline{\mathbf{R}},\omega)=-\omega^2\rho v_{\mathrm{P,S}}(\omega)\hat{\underline{\mathbf{v}}}_{\mathrm{P,S}}$$
$$\cdot\int\int\int_{V_{\mathrm{c}}}\chi_{\rho}(\underline{\mathbf{R}}')\mathrm{e}^{\mathrm{j}\underline{\mathbf{k}}_i^{\mathrm{P,S}}\cdot\underline{\mathbf{R}}'}\underline{\underline{\mathbf{\Gamma}}}(\underline{\mathbf{R}}-\underline{\mathbf{R}}',\omega)\mathrm{d}^3\underline{\mathbf{R}}'. \tag{3.33}$$

Since $\underline{\underline{\Gamma}}$ according to (2.34) is composed of a pressure wave term and a shear wave term we can concentrate on either one of them by either dot-multiplication with $\underline{\mathbf{K}}_{\mathrm{S}} + \underline{\mathbf{k}}_i^{\mathrm{P,S}}$ or cross-multiplication with $\underline{\mathbf{K}}_{\mathrm{P}} + \underline{\mathbf{k}}_i^{\mathrm{P,S}}$ and proceeding as with (3.26) to produce a P-image from P-wave incidence

$$\begin{aligned}&\left(\underline{\mathbf{K}}_{\mathrm{S}} + \underline{\mathbf{k}}_i^{\mathrm{P}}\right) \cdot \hat{\underline{\mathbf{v}}}_{\mathrm{s}}^{\mathrm{Born,P}}\left(K_x + k_{ix}^{\mathrm{P}}, K_y + k_{iy}^{\mathrm{P}}, d, \omega, \hat{\underline{\mathbf{v}}}_{\mathrm{P}}\right)\\ &= v_{\mathrm{P}}(\omega)\frac{\mathrm{j}}{2\left(K_{\mathrm{P}z} + k_{iz}^{\mathrm{P}}\right)^2}\mathrm{e}^{\mathrm{j}d\left(K_{\mathrm{P}z} + k_{iz}^{\mathrm{P}}\right)}\left(\underline{\mathbf{K}}_{\mathrm{S}} + \underline{\mathbf{k}}_i^{\mathrm{P}}\right)\\ &\quad \cdot \left(\underline{\mathbf{K}}_{\mathrm{P}} + \underline{\mathbf{k}}_i^{\mathrm{P}}\right)\left(\underline{\mathbf{K}}_{\mathrm{P}} + \underline{\mathbf{k}}_i^{\mathrm{P}}\right) \cdot \hat{\underline{\mathbf{v}}}_{\mathrm{P}}\tilde{\chi}_\rho(\underline{\mathbf{K}}),\end{aligned} \tag{3.34}$$

a (mode-converted) P-image from S-wave incidence

$$\begin{aligned}&\left(\underline{\mathbf{K}}_{\mathrm{S}} + \underline{\mathbf{k}}_i^{\mathrm{S}}\right) \cdot \hat{\underline{\mathbf{v}}}_{\mathrm{s}}^{\mathrm{Born,P}}\left(K_x + k_{ix}^{\mathrm{S}}, K_y + k_{iy}^{\mathrm{S}}, d, \omega, \hat{\underline{\mathbf{v}}}_{\mathrm{S}}\right)\\ &= v_{\mathrm{S}}(\omega)\frac{\mathrm{j}}{2\left(K_{\mathrm{P}z} + k_{iz}^{\mathrm{S}}\right)^2}\mathrm{e}^{\mathrm{j}d\left(K_{\mathrm{P}z} + k_{iz}^{\mathrm{S}}\right)}\left(\underline{\mathbf{K}}_{\mathrm{S}} + \underline{\mathbf{k}}_i^{\mathrm{S}}\right)\\ &\quad \cdot \left(\underline{\mathbf{K}}_{\mathrm{P}} + \underline{\mathbf{k}}_i^{\mathrm{S}}\right)\left(\underline{\mathbf{K}}_{\mathrm{P}} + \underline{\mathbf{k}}_i^{\mathrm{S}}\right) \cdot \hat{\underline{\mathbf{v}}}_{\mathrm{S}}\tilde{\chi}_\rho(\underline{\mathbf{K}});\end{aligned} \tag{3.35}$$

similarly an S-image from S-wave incidence

$$\begin{aligned}&\left(\underline{\mathbf{K}}_{\mathrm{P}} + \underline{\mathbf{k}}_i^{\mathrm{S}}\right) \times \hat{\underline{\mathbf{v}}}_{\mathrm{s}}^{\mathrm{Born,S}}\left(K_x + k_{ix}^{\mathrm{S}}, K_y + k_{iy}^{\mathrm{S}}, d, \omega, \hat{\underline{\mathbf{v}}}_{\mathrm{S}}\right)\\ &= -k_{\mathrm{S}}^2 v_{\mathrm{S}}(\omega)\frac{\mathrm{j}}{2\left(K_{\mathrm{S}z} + k_{iz}^{\mathrm{S}}\right)^2}\mathrm{e}^{\mathrm{j}d\left(K_{\mathrm{S}z} + k_{iz}^{\mathrm{S}}\right)}\left(\underline{\mathbf{K}}_{\mathrm{P}} + \underline{\mathbf{k}}_i^{\mathrm{S}}\right)\\ &\quad \times \left[\underline{\underline{\mathbf{I}}} - \frac{1}{k_{\mathrm{S}}^2}\left(\underline{\mathbf{K}}_{\mathrm{S}} + \underline{\mathbf{k}}_i^{\mathrm{S}}\right)\left(\underline{\mathbf{K}}_{\mathrm{S}} + \underline{\mathbf{k}}_i^{\mathrm{S}}\right)\right] \cdot \hat{\underline{\mathbf{v}}}_{\mathrm{S}}\tilde{\chi}_\rho(\underline{\mathbf{K}})\end{aligned} \tag{3.36}$$

and a (mode-converted) S-image from P-wave incidence

$$\begin{aligned}&\left(\underline{\mathbf{K}}_{\mathrm{P}} + \underline{\mathbf{k}}_i^{\mathrm{P}}\right) \times \hat{\underline{\mathbf{v}}}_{\mathrm{s}}^{\mathrm{Born,S}}\left(K_x + k_{ix}^{\mathrm{P}}, K_y + k_{iy}^{\mathrm{P}}, d, \omega, \hat{\underline{\mathbf{v}}}_{\mathrm{P}}\right)\\ &= -k_{\mathrm{S}}^2 v_{\mathrm{P}}(\omega)\frac{\mathrm{j}}{2\left(K_{\mathrm{S}z} + k_{iz}^{\mathrm{P}}\right)^2}\mathrm{e}^{\mathrm{j}d\left(K_{\mathrm{S}z} + k_{iz}^{\mathrm{P}}\right)}\left(\underline{\mathbf{K}}_{\mathrm{P}} + \underline{\mathbf{k}}_i^{\mathrm{P}}\right)\\ &\quad \times \left[\underline{\underline{\mathbf{I}}} - \frac{1}{k_{\mathrm{S}}^2}\left(\underline{\mathbf{K}}_{\mathrm{S}} + \underline{\mathbf{k}}_i^{\mathrm{P}}\right)\left(\underline{\mathbf{K}}_{\mathrm{S}} + \underline{\mathbf{k}}_i^{\mathrm{P}}\right)\right] \cdot \hat{\underline{\mathbf{v}}}_{\mathrm{P}}\tilde{\chi}_\rho(\underline{\mathbf{K}})\end{aligned} \tag{3.37}$$

can be obtained. Note the similarity of the transverse ⇒ transverse wave algorithm (3.36) with the electromagnetic counterpart (3.26)! The respective $\underline{\mathbf{K}}$-space vectors in (3.3)–(3.37) are defined as follows:

$$\underline{\mathbf{K}}_{\mathrm{P,S}} = K_x\underline{\mathbf{e}}_x + K_y\underline{\mathbf{e}}_y + K_{\mathrm{P,S}z}\underline{\mathbf{e}}_z, \tag{3.38}$$

$$K_{\mathrm{P,S}z} = \sqrt{k_{\mathrm{P,S}}^2 - \left(K_x + k_{ix}^{\mathrm{P,S}}\right)^2 - \left(K_y + k_{iy}^{\mathrm{P,S}}\right)^2} - k_{iz}^{\mathrm{P,S}}. \tag{3.39}$$

Of course, if data strictly satisfy the Born approximation, each of the above inversion equations yields the same result; yet in real life, data are not strictly of the Born type, and, therefore, application of different inversion equations might yield complementary information about the scatterer.

4. Electromagnetic wave field modeling and inversion

In Fig. 1 the real-life test specimen is complemented by a computer model ready for computational simulations; for electromagnetic wave calculations we use the commercially available code Microwave Studio [13] whose primary output is the time evolution of spatially distributed wave amplitudes, i.e., time domain wave fronts. Fig. 5 shows two respective snap-shots: a plane wave with polarization $\hat{\underline{\mathbf{E}}}_0$ parallel to the duct axis is running from top to bottom, which is scattered by the tendon duct and the reinforcement

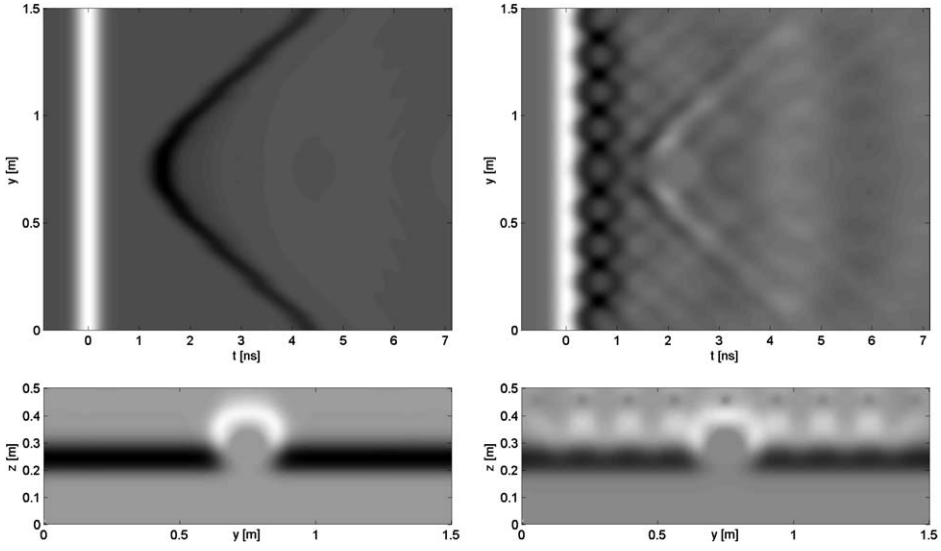

Fig. 5. Bottom: Impulsive electromagnetic wave front snap-shots for two cross-sections of the computer specimen displayed in Fig. 1; left: cross-section without reinforcement; right: cross-section with reinforcement (horizontal axis: time, vertical axis: scan-coordinate); top: B-scan data for these wave fields (horizontal axis: time, vertical axis: scan coordinate).

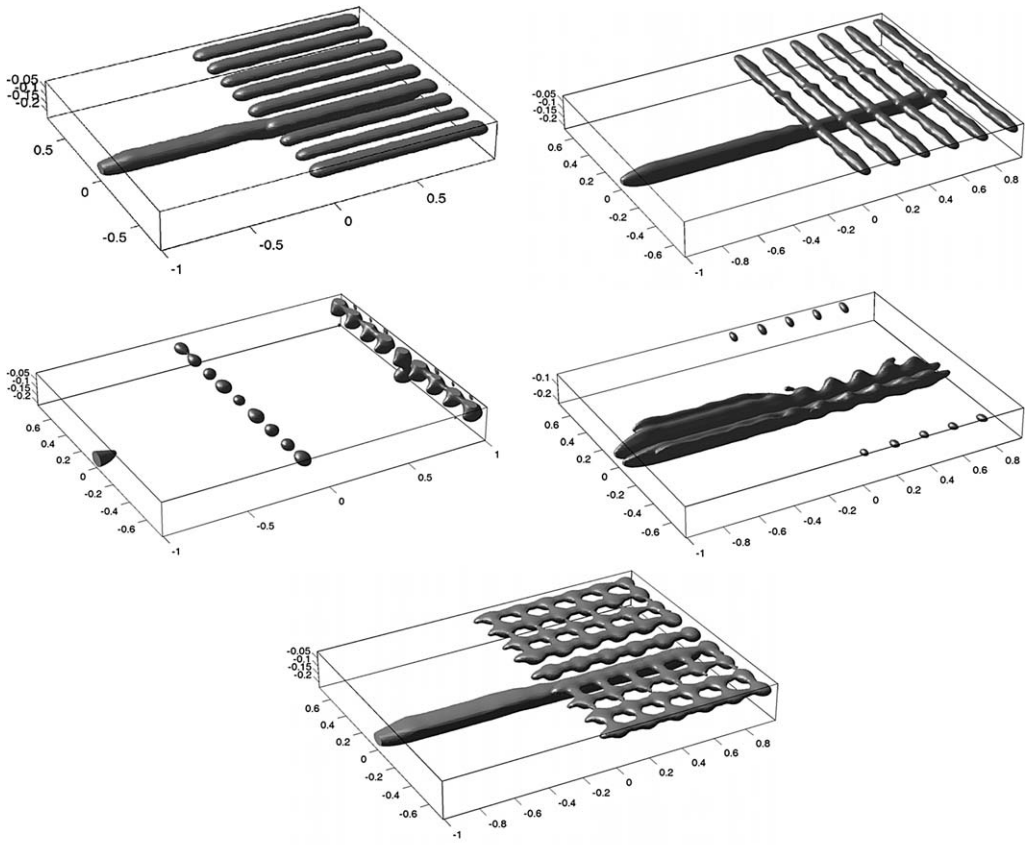

Fig. 6. Electromagnetic vector wave inversion for the computer specimen displayed in Fig. 1; top: $\underline{\gamma}_u(\underline{\mathbf{R}}) \cdot \widehat{\underline{\mathbf{E}}}_0$ and $\underline{\gamma}_u(\underline{\mathbf{R}}) \cdot \widehat{\underline{\mathbf{E}}}_{\text{orth}}$; middle: $\underline{\gamma}_u(\underline{\mathbf{R}}) \cdot \hat{\underline{\mathbf{k}}}_i$ for $\widehat{\underline{\mathbf{E}}}_0$-polarization and $\underline{\gamma}_u(\underline{\mathbf{R}}) \cdot \hat{\underline{\mathbf{k}}}_i$ for $\widehat{\underline{\mathbf{E}}}_{\text{orth}}$-polarization; bottom: magnitude of $\underline{\gamma}_u(\underline{\mathbf{R}})$ obtained from above components.

grid, both modeled with infinite electrical conductivity embedded in homogeneous cement. We have selected two cross-sections out of the three-dimensional wave field, one on the side with no reinforcement and one on the side with reinforcement, the latter one clearly exhibiting the disturbance caused by the grid. In addition, Fig. 5 displays two cross-sections out of the resulting three-dimensional B-scan data field in the component parallel to $\widehat{\underline{\mathbf{E}}}_0$, again one without and one with the reinforcement grid: The first data line reflects the incident plane wave followed by either the clean hyperbola (cross-section of a hyperboloid) representing the tendon duct scattering or the respective hyperbola disturbed by the grid together with superimposed hyperbolas of the single grid cylinders. After a Fourier transform with regard to time yielding data spectra the complete three-dimensional polarimetric data field is now ready for inversion, i.e., the three-dimensional components $\underline{\gamma}_u(\underline{\mathbf{R}}) \cdot \widehat{\underline{\mathbf{E}}}_0$ and $\underline{\gamma}_u(\underline{\mathbf{R}}) \cdot \hat{\underline{\mathbf{k}}}_i$ ($\hat{\underline{\mathbf{k}}}_i$ being orthogonal to the specimen surface) can be deduced from (3.29); they are displayed as *iso*-contour plots in Fig. 6: Typically, for $\widehat{\underline{\mathbf{E}}}_0$ parallel to the duct axis only those grid cylinders having the same orientation are "visible" by the incident wave, and $\hat{\underline{\mathbf{k}}}_i$-components of the induced current appear only at the end points of the duct and the grid bars. The opposite is true if the polarization of the incident wave is changed to $\widehat{\underline{\mathbf{E}}}_{\text{orth}}$, because in that case circumferential currents are induced on the duct surface (Fig. 5). From $\underline{\gamma}_u(\underline{\mathbf{R}}) \cdot \widehat{\underline{\mathbf{E}}}_0$, $\underline{\gamma}_u(\underline{\mathbf{R}}) \cdot \widehat{\underline{\mathbf{E}}}_{\text{orth}}$ and the average of $\underline{\gamma}_u(\underline{\mathbf{R}}) \cdot \hat{\underline{\mathbf{k}}}_i$ as calculated for both polarizations the magnitude of the singular function is obtained as displayed in Fig. 5. Obviously, simulations of that kind allow for parametric studies relating to the mesh size of the reinforcement grid below which tendon ducts can still be located.

5. Elastic wave field modeling, measurement and inversion

5.1. Synthetic data

We have already tested (3.34) and (3.37) (in a somewhat different version according to a somewhat different derivation exploiting far-field properties) against experimental data obtained for side-wall drilled holes as defects in a steel test specimen [9]. It turns out that both images indeed provide complementary information about the scatterers. Here, we will demonstrate that with two-dimensional synthetic data obtained for a tendon duct model. Regarding the numerical computation of elastodynamic wave propagation, based on the similarity of the underlying governing equations, we apply the same discretization idea as implemented in microwave studio (the finite integration technique) yet we use our own code [12]. Fig. 7 displays geometry, wave fronts, B-scan data and images for a

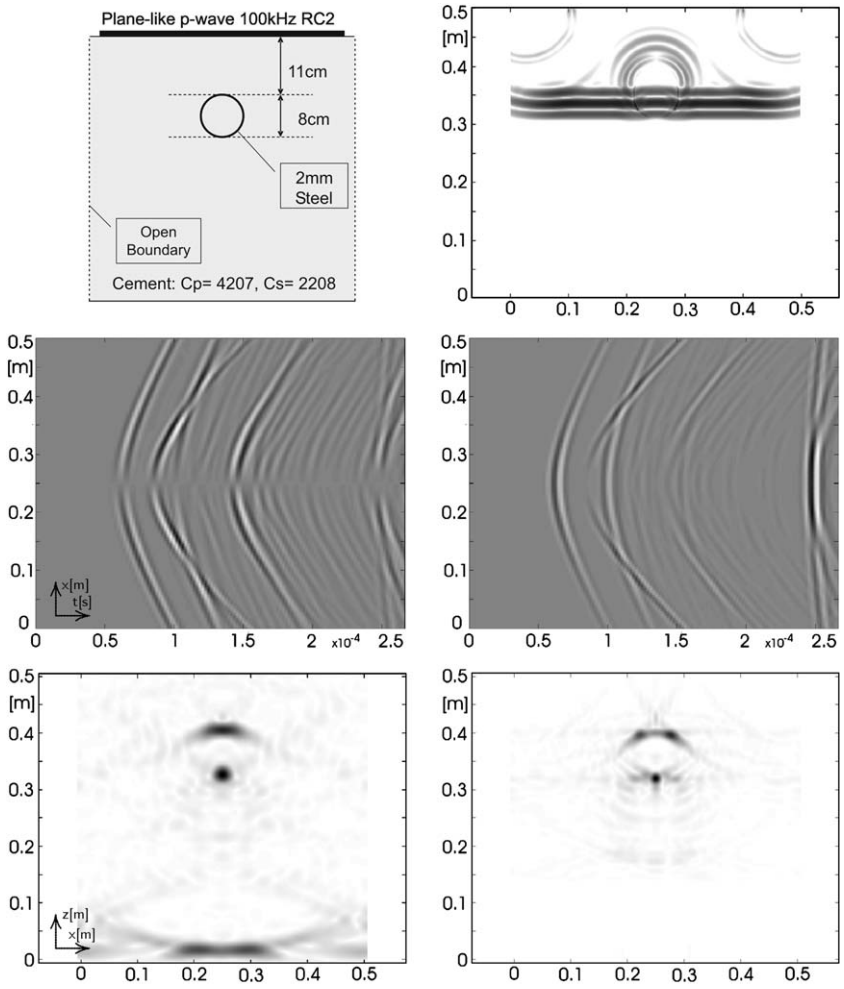

Fig. 7. Two-dimensional elastic wave field modeling and inversion: Geometry of the specimen, wave front snap-shot, B-scan data for the data component normal and tangential to the surface (horizontal axis: time, vertical axis: scan coordinate), P ⇒ P-image, P ⇒ S-image.

tendon duct related model; it consists of a circular cylindrical steel shell containing cement being embedded in homogeneous cement. The bar on top of the specimen surface indicates the transducer aperture, which vertically radiates a nearly plane pressure wave; when scattered by the duct geometry, ''reflected'' pressure and shear waves are created—the latter can be recognized by the zero in backscattering direction—traveling back to the surface, where they are supposed to be recorded pointwise (the spherical waves emanating from the top edges of the specimen are created by Rayleigh surface waves from the edges of the radiating aperture). The two B-scans below show the normal component

Fig. 8. Real-life experiment with elastic waves: Autobahn bridge near Vienna; scanning device with A1220 55 KHz shear wave combined transducer array.

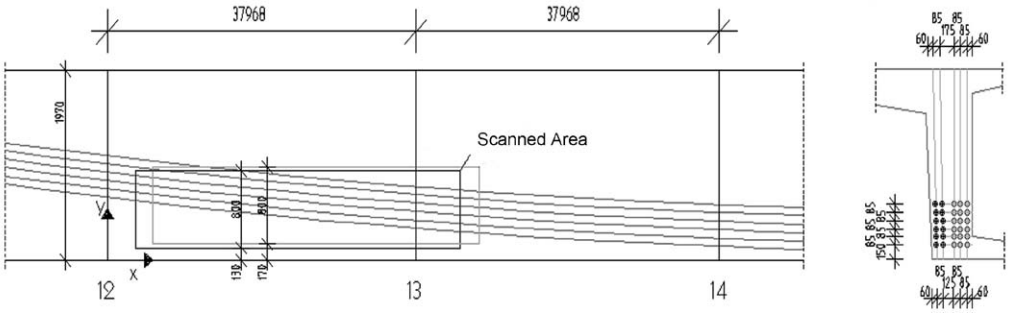

Fig. 9. Scan area: top view and side view (the 30 ducts have diameters of 40 mm each containing a single steel cable with a diameter of 32 mm).

of the particle velocity vector (left) and its component tangential to the surface (right). Typically, one recognizes scattering hyperbolas as in the electromagnetic case (Fig. 5), here in particular two pressure wave hyperbolas coming from the front and rear surface of the duct model, as well as mode-converted shear wave hyperbolas to be recognized by the different asymptotic slopes. After a Fourier transform with regard to time, these data can be inserted into the two-dimensional versions ($K_y = 0$) of (3.34) and (3.37) to produce P $\Rightarrow$ P- and P $\Rightarrow$ S-images, respectively. Fig. 7 confirms that there is complementary information about the duct surface in those two images.

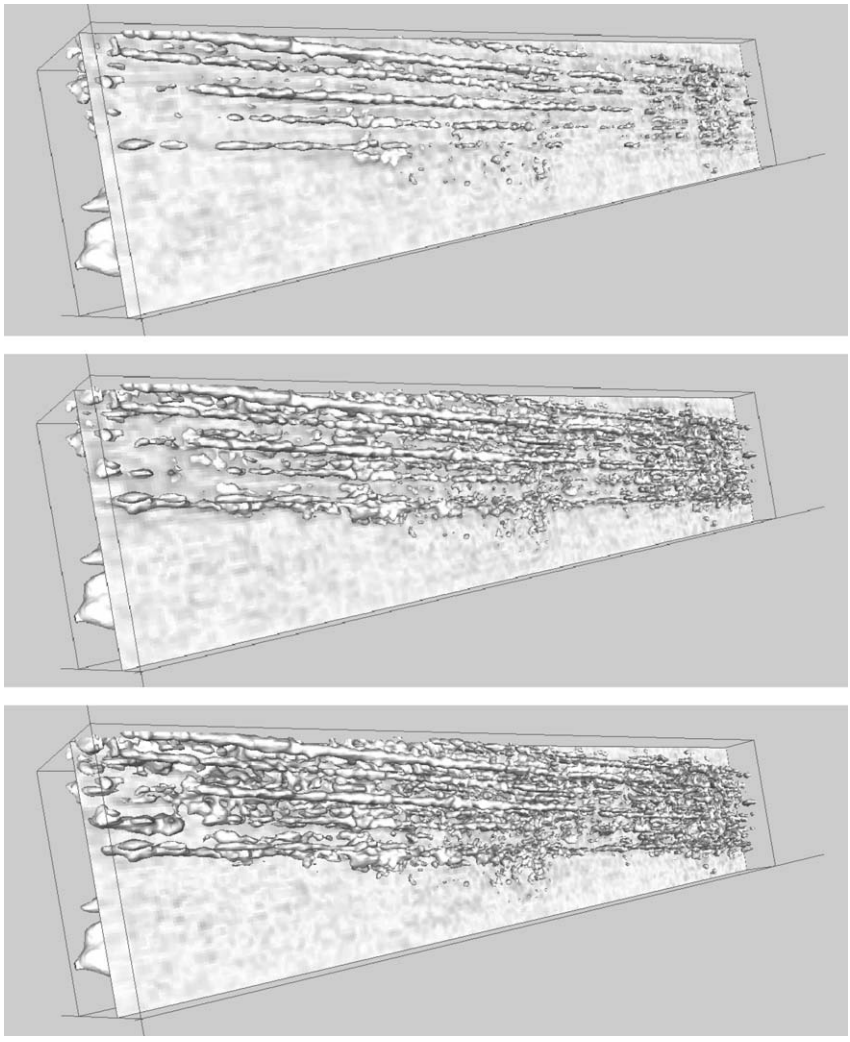

Fig. 10. 55 KHz multi-monostatic scalar shear wave image of tendon ducts; note: the plane attached to the three-dimensional image space slides down from the top in the sequence of pictures (12 cm, 14 cm, 18 cm).

5.2. Experimental real-life data

With Fig. 8 we enter the field of real-life applications of the "image producing theory" as outlined above; it shows part of an Autobahn bridge near Vienna in Austria where the German Federal Institute for Materials Research and Testing[1] took on-site measurements with the A1220 point-contact transducer from ACS (acoustic control systems) in a multi-monostatic shear wave mode within a pre-selected area. The resulting three-dimensional data field in terms of $\hat{\underline{\mathbf{v}}}_S \cdot \underline{\mathbf{v}}_s^S(x,y,d,\omega,\hat{\underline{\mathbf{v}}}_S)$ was treated as a scalar data field and processed according to the algorithm outlined in Section 3.2.2. The scan area is shown in Fig. 9; below that area five layers of tendon ducts each containing six specimens are "hidden", and the imaging results as displayed in Fig. 10 clearly show that at least three layers are prone to detection at their respective location.

6. Conclusions

Based on the similarity of the underlying governing equations we have evaluated a unified theory of modeling and imaging with acoustic, electromagnetic and elastic waves to be applied to specific problems in nondestructive testing of concrete. For additional examples the reader is referred to [10,11]. Our goal in the near future will be the further exploitation of the polarimetric information of electromagnetic and elastic waves, in particular utilizing the various elastic wave modes for which the A1220 transducer can be operational, in order to be finally able not only to detect tendon ducts but to assess their integrity related to grouting defects.

References

[1] de Hoop AT. Handbook of radiation and scattering of waves. London: Academic Press; 1995.
[2] Karlsson A, Kristensson G. Constitutive relations, dissipation and reciprocity for the Maxwell equations in the time domain. J Electrom Waves Appl 1992;6:537.
[3] Belkebir K, Saillard M. Special section: Testing inversion algorithms against experimental data. Inverse Probl 2001;17.
[4] Langenberg KJ. Linear scalar inverse scattering. In: Pike R, Sabatier PC, editors. Scattering in pure and applied science. London: Academic Press; 2002.
[5] Langenberg KJ, Brandfaß M, Hannemann R, Hofmann C, Kaczorowski T, Kostka J, et al. Inverse scattering with acoustic, electromagnetic and elastic waves as applied in nondestructive evaluation. In: Wirgin A, editor. Wavefield inversion. Vienna: Springer; 1999.
[6] Marklein R, Mayer K, Hannemann R, Krylow T, Balasubramanian K, Langenberg KJ, et al. Linear and nonlinear inversion algorithms applied in nondestructive evaluation. Inverse Probl 2002;18:1733.
[7] Chen HC. Theory of electromagnetic waves. New York: McGraw-Hill; 1983.
[8] Langenberg KJ, Brandfaß M, Fellinger P, Gurke T, Kreutter T. A unified theory of multidimensional electromagnetic vector inverse scattering within the Kirchhoff or Born approximation. In: Boerner WM, Überall H, editors. Radar target imaging. Berlin: Springer; 1994.
[9] Kostka J, Langenberg KJ, Mayer K, Krause M. Improved flaw imaging applying elastodynamic far-field Fourier inversion (EL-FT-SAFT). In: Proc 2nd int conf on computer methods and inverse problems in nondestructive testing and diagnostics, Minsk, October 1998, p. 397.
[10] Langenberg KJ, Marklein R, Mayer K, Krylow T, Ampha P, Krause M, et al. Wavefield inversion in nondestructive testing. In: Pinto IM, Galdi V, Felsen LB, editors. Electromagnetics in a complex world. Berlin: Springer; 2004.
[11] Langenberg KJ, Marklein R, Mayer K, Wiggenhauser H, Krause M. Multimode modeling and imaging in nondestructive testing. In: Russer P, Mongiardo M, editors. Fields, networks, computational methods, and systems in modern electrodynamics. Berlin: Springer; 2004.
[12] Marklein R. The finite integration technique as a general tool to compute acoustic, electromagnetic, elastodynamic and coupled wave fields. In: Stone WR, editor. Review of radio science 1999–2002. Piscataway: IEEE Press; 2002.
[13] www.cst.de.
[14] www.for384.uni-stuttgart.de.

[1] We gratefully acknowledge the cooperation with Dr. H. Wiggenhauser, Dr. M. Krause and D. Streicher, who made these data available to us through a joint research project funded by the German Research Council [14].